Progress In Electromagnetics Research, Vol. 152, 77–93, 2015

Sparse Electromagnetic Imaging Using Nonlinear Landweber Iterations

Abdulla Desmal and Hakan Bağcı*

Abstract—A scheme for efficiently solving the nonlinear electromagnetic inverse scattering problem on sparse investigation domains is described. The proposed scheme reconstructs the (complex) dielectric permittivity of an investigation domain from fields measured away from the domain itself. Least-squares data misfit between the computed scattered fields, which are expressed as a nonlinear function of the permittivity, and the measured fields is constrained by the L_0/L_1-norm of the solution. The resulting minimization problem is solved using nonlinear Landweber iterations, where at each iteration a thresholding function is applied to enforce the sparseness-promoting L_0/L_1-norm constraint. The thresholded nonlinear Landweber iterations are applied to several two-dimensional problems, where the "measured" fields are synthetically generated or obtained from actual experiments. These numerical experiments demonstrate the accuracy, efficiency, and applicability of the proposed scheme in reconstructing sparse profiles with high permittivity values.

1. INTRODUCTION

Electromagnetic inverse scattering problem is defined as finding unknown material properties, such as dielectric permittivity or conductivity or both, in an investigation domain from scattered fields measured away from the domain itself [1–3]. Numerical methods for solving the inverse scattering problem are called for in various applications in engineering including but not limited to through-wall and tomography imaging [4–6], non-destructive testing [7], crack/mine detection [8, 9], hydrocarbon reservoir exploration and monitoring [10, 11], and radar and remote sensing [12–14]. Despite the vast amount of application areas, formulating and implementing efficient and accurate inverse solvers is still a challenging task. This can be attributed to two essential characteristics of the inverse scattering problem. (i) Nonlinearity: Scattered field is a nonlinear function of the permittivity. The strength of the nonlinearity increases with the value of the permittivity [1]. (ii) Ill-posedness: Integral operators used for expressing the scattered fields in terms of the permittivity have a "smoothening" effect. Smoothening combined with the facts that the number of measurements is finite and the measurements are noisy makes the inverse scattering problem ill-posed [1–3, 5].

Methods for solving the electromagnetic inverse problem can be classified based on the level of maximum permittivity they can "handle", i.e., the strength of the nonlinearity in the scattering equations. For low values of permittivity, first-order linearization methods, such as the first-order Born and Rytov approximations, provide a convergent and satisfactorily accurate solution [15]. Even though higher-order schemes, such as the extended-Born [16] and second-order Born approximations [17] and the Born iterative method [18–20], are applicable for higher values of permittivity when compared to the first-order linearization methods, they still fail to produce convergent solutions for many practical engineering applications where investigation domains involve "strong" scatterers with high values of

Received 28 May 2015, Accepted 27 July 2015, Scheduled 29 July 2015

* Corresponding author: Hakan Bağcı (hakan.bagci@kaust.edu.sa).
The authors are with the Division of Computer, Electrical, and Mathematical Sciences and Engineering (CEMSE), King Abdullah University of Science and Technology (KAUST), Thuwal 23955-6900, Saudi Arabia.

permittivity. This drawback can be overcome by developing "complete" nonlinear inversion schemes that do not linearize the forward scattering equations. Examples of these schemes include Newton-type methods such as the inexact Newton [21–23], distorted Born [24], and Levenberg-Marquardt [25] methods. Additionally, other schemes making use of the nonlinear conjugate gradient [26–29] or the steepest descent [30, 31] are widely used for image reconstruction with strong scatterers.

The ill-posedness is alleviated by constructing the inverse problem in the form of a minimization problem for the data misfit between the measured and the computed scattered fields, which is constrained by adding a regularization/penalty term [2, 3]. Data misfit is represented in the L_2-norm (i.e., least-squares fit) and the penalty term can be the L_0-, L_1-, or L_2-norm of the solution [2, 3]. The L_2-norm penalty term, which has been the more commonly used one, promotes smoothness in the solution [3]. On the other hand, solving the minimization problem regularized with the L_0/L_1-norm penalty term promotes sharpness and sparseness, i.e., discontinuities in the recovered solution are detected more accurately [32, 33]. It should be noted here that minimization problems with the sparseness-promoting L_0- and L_1-norm penalty terms have often been studied in linear or linearized ill-posed problems. Their use in electromagnetic inverse problems has been limited to only the Born iterative [19, 20] and inexact Newton [21] methods even though sparse domains are very common in non-destructive testing, through-wall, and radar imaging [6–9, 19–21, 34].

In this work, to enable efficient and accurate electromagnetic imaging of the sparse domains involving strong scatterers, nonlinear least-squares data misfit between the measured scattered fields and the computed ones, which are expressed directly as a nonlinear function of the permittivity, is constrained by the sparseness-promoting L_0- and L_1-norm penalty terms. The resulting minimization problem, which is also referred as sparsity-constrained nonlinear Tikhonov problem, is solved using nonlinear Landweber (NLW) iterations [35, 36], where at each iteration a thresholding function is applied to enforce the sparsity constraint. Unlike inexact Newton [21] and Born iterative [19, 20] methods with sparsity constraints, the proposed scheme avoids generation of a sequence of linear sparse optimization problems and requires only one regularization parameter, which directly penalizes the nonlinear problem, to be set. Consequently, it simplifies the task of heuristic parameter "tweaking", which is oftentimes very cumbersome for existing inversion algorithms. Application of the proposed scheme to several two-dimensional (2-D) problems, where the "measured" fields are synthetically generated or obtained from actual experiments, demonstrates that the proposed scheme (i) produces sharper and more accurate reconstruction of permittivity profiles in sparse domains (in comparison with schemes which use L_2-norm regularization) and (ii) maintains its convergence during the reconstruction of profiles with higher permittivity values (in comparison with schemes which make use of (iterative) linearization of the nonlinear problem).

The rest of the paper is organized as follows. Section 2.1 presents the nonlinear 2-D electromagnetic scattering equations, Section 2.2 describes a scheme to discretize the scattering equations and constructs the nonlinear forward solver, Section 2.3 focuses on the sparsity-constrained minimization problem and its solution using the thresholded NLW iterations, and Section 2.4 describes a frequency hopping scheme to be used together with the NLW iterations under excitations with multiple frequencies. Section 3 presents numerical experiments, which demonstrate the efficiency, accuracy, and applicability of the proposed scheme in reconstructing the permittivity profiles in sparse domains with strong scatterers. Finally, Section 4 concludes with a summary and future research directions.

2. FORMULATION

2.1. Nonlinear Scattering Equations

Let S represent the support of the 2-D investigation domain residing in an unbounded homogenous background medium (Figure 1). The permeability and the (complex) permittivity of the investigation domain and the background medium are represented by $\{\mu_0, \varepsilon(\mathbf{r})\}$ and $\{\mu_0, \varepsilon_0\}$, respectively. Here, $\varepsilon(\mathbf{r})$ is the unknown to be determined. The investigation domain is surrounded by a transmitter and N^R receivers (Figure 1). Let ω and $E_u^{inc}(\mathbf{r})$, $u \in \{x, y, z\}$ represent the frequency of the transmitter and the three components of the incident electric field it generates. Upon excitation, electric current density with three components $J_u(\mathbf{r})$, $u \in \{x, y, z\}$ is induced on S. These current density components satisfy $J_u(\mathbf{r}) = j\omega\varepsilon_0\tau(\mathbf{r})E_u(\mathbf{r})$. Here, $E_u(\mathbf{r})$ are the three components of the total electric field and $\tau(\mathbf{r})$

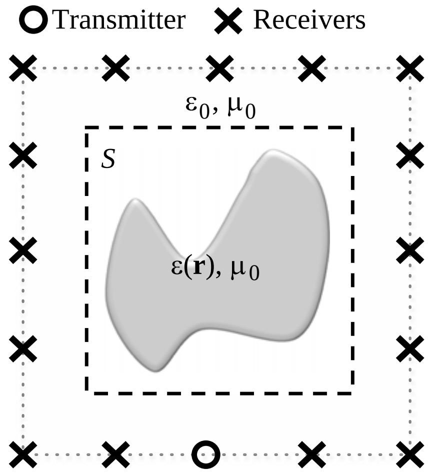

Figure 1. Description of the 2-D electromagnetic inverse scattering problem.

is the dielectric contrast defined as

$$\tau(\mathbf{r}) = \begin{cases} \varepsilon(\mathbf{r})/\varepsilon_0 - 1, & \mathbf{r} \in S \\ 0, & \text{else} \end{cases}.$$

Let $E_u^{sca}(\mathbf{r})$, $u \in \{x, y, z\}$ represent the three components of the scattered electric field generated by the electric current density induced on S. Considering TE ($u \in \{x, y\}$) and TM ($u = z$) field interactions separately, $E_u^{sca}(\mathbf{r})$ are expressed as

$$\begin{aligned} E_x^{sca}(\mathbf{r}) &= -\tau(\mathbf{r})E_x(\mathbf{r}) + \frac{c_0^2}{j\omega}\left[\partial_{xy}^2 A_y(\mathbf{r}) - \partial_{yy}^2 A_x(\mathbf{r})\right], \\ E_y^{sca}(\mathbf{r}) &= -\tau(\mathbf{r})E_y(\mathbf{r}) + \frac{c_0^2}{j\omega}\left[\partial_{xy}^2 A_x(\mathbf{r}) - \partial_{xx}^2 A_y(\mathbf{r})\right], \\ E_z^{sca}(\mathbf{r}) &= j\omega A_z(\mathbf{r}). \end{aligned} \tag{1}$$

Here, $A_u(\mathbf{r})$, $u \in \{x, y, z\}$ are the three components of the magnetic vector potential, which are expressed as

$$A_u(\mathbf{r}) = \mu_0 \int_S J_u(\mathbf{r}')G(\mathbf{r}, \mathbf{r}')ds' = \frac{j\omega}{c_0^2}\int_S \tau(\mathbf{r}')E_u(\mathbf{r}')G(\mathbf{r}, \mathbf{r}')ds'$$

and $G(\mathbf{r}, \mathbf{r}') = H_0^{(2)}(k_0|\mathbf{r} - \mathbf{r}'|)/(4j)$, $k_0 = \omega\sqrt{\varepsilon_0\mu_0}$, and $c_0 = 1/\sqrt{\mu_0\varepsilon_0}$ are the 2-D Green function, wave number, and speed of light in the background medium, respectively.

Inserting (1) into the fundamental field relation $E_u^{inc}(\mathbf{r}) = E_u(\mathbf{r}) - E_u^{sca}(\mathbf{r})$ and enforcing the resulting equation on $\mathbf{r} \in S$ yields three integral equations that relate $\tau(\mathbf{r})$ to $E_u(\mathbf{r})$ [37]:

$$\begin{aligned} E_x^{inc}(\mathbf{r}) &= \left[1 + \tau(\mathbf{r})\right]E_x(\mathbf{r}) - \frac{c_0^2}{j\omega}\left[\partial_{xy}^2 A_y(\mathbf{r}) - \partial_{yy}^2 A_x(\mathbf{r})\right], \quad \mathbf{r} \in S, \\ E_y^{inc}(\mathbf{r}) &= \left[1 + \tau(\mathbf{r})\right]E_y(\mathbf{r}) - \frac{c_0^2}{j\omega}\left[\partial_{xy}^2 A_x(\mathbf{r}) - \partial_{xx}^2 A_y(\mathbf{r})\right], \quad \mathbf{r} \in S, \\ E_z^{inc}(\mathbf{r}) &= E_z(\mathbf{r}) - j\omega A_z(\mathbf{r}), \quad \mathbf{r} \in S. \end{aligned} \tag{2}$$

It should be clear from (2) that the relation between $E_u(\mathbf{r})$ and $\tau(\mathbf{r})$ is nonlinear. If $\tau(\mathbf{r})$ were known, (2), which describes a linear relation between $E_u(\mathbf{r})$ and $E_u^{inc}(\mathbf{r})$, could be easily solved for $E_u(\mathbf{r})$.

Let $\mathbf{r}_m^R$, $m = 1, \ldots, N^R$, represent the locations of the receivers surrounding the investigation domain. Note that $\mathbf{r}_m^R \notin S$ and $\tau(\mathbf{r}_m^R) = 0$. Then, sampling (1) at $\mathbf{r}_m^R$ yields:

$$E_x^{sca}(\mathbf{r}_m^R) = \frac{c_0^2}{j\omega}\left[\partial_{xy}^2 A_y(\mathbf{r})\big|_{\mathbf{r}=\mathbf{r}_m^R} - \partial_{yy}^2 A_x(\mathbf{r})\big|_{r=\mathbf{r}_m^R}\right],$$

$$E_y^{sca}(\mathbf{r}_m^R) = \frac{c_0^2}{j\omega}\left[\partial_{xy}^2 A_x(\mathbf{r})\big|_{\mathbf{r}=\mathbf{r}_m^R} - \partial_{xx}^2 A_y(\mathbf{r})\big|_{\mathbf{r}=\mathbf{r}_m^R}\right], \tag{3}$$
$$E_z^{sca}(\mathbf{r}_m^R) = j\omega A_z(\mathbf{r}_m^R).$$

In the set-up described here, the inverse problem is defined as finding the unknown $\tau(\mathbf{r})$ from the scattered fields *measured* by the receivers. Let $E_u^{mea}(\mathbf{r}_m^R)$ represent the components of these fields. Then, $\tau(\mathbf{r})$ can be extracted by minimizing the data misfit between $E_u^{sca}(\mathbf{r}_m^R)$ given by (3) and the measured samples $E_u^{mea}(\mathbf{r}_m^R)$. It should be noted here that the number of measurements N^R is finite. Additionally, convolution integrals between $\tau(\mathbf{r}')E_u(\mathbf{r}')$ and $G(\mathbf{r},\mathbf{r}')$ in (2) and (3) have a "smoothening" effect on the fast varying components of $\tau(\mathbf{r}')$ and $E_u(\mathbf{r}')$, which results in loss of information especially if $E_u^{mea}(\mathbf{r}_m^R)$ are obtained from "noisy" measurements. These two factors make the inverse problem ill posed [1–3]. Furthermore, a closer look at (2) and (3) reveals that $E_u^{sca}(\mathbf{r}_m^R)$ are nonlinear functions of $\tau(\mathbf{r})$ meaning that the inverse problem is nonlinear in $\tau(\mathbf{r})$.

2.2. Discretization

To numerically solve the inverse scattering problem described in the previous section, (2) and (3) should be discretized. To this end, support S is divided into N square cells with dimension Δd. It is assumed that Δd is small enough to resolve the variations in $\tau(\mathbf{r})$ and $E_u(\mathbf{r})$, $u \in \{x, y, z\}$. Under this assumption, $\tau(\mathbf{r})$ and $E_u(\mathbf{r})$ are approximated as:

$$\tau(\mathbf{r}) = \sum_{k=1}^{N} \{\bar{t}\}_k p_k(\mathbf{r}), \quad E_u(\mathbf{r}) = \sum_{k=1}^{N} \{\bar{E}_u\}_k p_k(\mathbf{r}). \tag{4}$$

Here, $\bar{t}$ and $\bar{E}_u$ are $N \times 1$ vectors storing the samples of $\tau(\mathbf{r})$ and $E_u(\mathbf{r})$, i.e., $\{\bar{t}\}_k = \tau(\mathbf{r}_k)$, $\{\bar{E}_u\}_k = E_u(\mathbf{r}_k)$, where $\mathbf{r}_k$ are the centers of the cells, and $p_k(\mathbf{r})$ is the pulse basis function defined on the kth cell as

$$p_k(\mathbf{r}) = \begin{cases} 1, & \mathbf{r} \in S_k \\ 0, & \text{else} \end{cases}$$

and S_k is the support of the kth cell. Inserting (4) into (2) and evaluating the resulting equation at $\mathbf{r}_j$, $j = 1, \ldots, N$ yield a system of equations:

$$\bar{E}^{inc} = \bar{F}\bar{E}. \tag{5}$$

Here, $\bar{E}^{inc}$ and $\bar{E}$ are $3N \times 1$ vectors, and $\bar{F}$ is a $3N \times 3N$ matrix, which are expressed in terms of other vectors and matrices as

$$\bar{E}^{inc} = \begin{bmatrix} \bar{E}_x^{inc} \\ \bar{E}_y^{inc} \\ \bar{E}_z^{inc} \end{bmatrix}, \quad \bar{E} = \begin{bmatrix} \bar{E}_x \\ \bar{E}_y \\ \bar{E}_z \end{bmatrix}, \quad \bar{F} = \begin{bmatrix} \bar{I} + \left(\bar{I} + \bar{G}_{yy}\right) D\left(\bar{t}\right) & -\bar{G}_{xy} D\left(\bar{t}\right) & 0 \\ -\bar{G}_{xy} D\left(\bar{t}\right) & \bar{I} + \left(\bar{I} + \bar{G}_{xx}\right) D\left(\bar{t}\right) & 0 \\ 0 & 0 & \bar{I} + k_0^2 \bar{G} D\left(\bar{t}\right) \end{bmatrix}. \tag{6}$$

In (6), $\bar{E}_u^{inc}$ and $\bar{E}_u$ are $N \times 1$ vectors storing samples of $E_u^{inc}(\mathbf{r})$ and $E_u(\mathbf{r})$ on S, i.e., $\{\bar{E}_u\}_k = E_u(\mathbf{r}_k)$, $k = 1, \ldots, N$, $\bar{I}$ is the $N \times N$ identity matrix, the operator $D(\cdot)$ generates a diagonal matrix with entries equal to those of its argument vector; and $\bar{G}$, $\bar{G}_{xx}$, $\bar{G}_{xy}$, and $\bar{G}_{yy}$ are $N \times N$ matrices storing the samples of the convolution between $p_k(\mathbf{r}')$ and $G(\mathbf{r},\mathbf{r}')$, $\partial_{xx}^2 G(\mathbf{r},\mathbf{r}')$, $\partial_{xy}^2 G(\mathbf{r},\mathbf{r}')$, and $\partial_{yy}^2 G(\mathbf{r},\mathbf{r}')$, i.e.,

$$\left\{\bar{G}\right\}_{jk} = \int_{S_k} G\left(\mathbf{r}_j, \mathbf{r}'\right) ds',$$
$$\left\{\bar{G}_{xx}\right\}_{jk} = \int_{S_k} \partial_{xx}^2 G\left(\mathbf{r}, \mathbf{r}'\right)\big|_{\mathbf{r}=\mathbf{r}_j} ds',$$
$$\left\{\bar{G}_{xy}\right\}_{jk} = \int_{S_k} \partial_{xy}^2 G\left(\mathbf{r}, \mathbf{r}'\right)\big|_{\mathbf{r}=\mathbf{r}_j} ds',$$
$$\left\{\bar{G}_{yy}\right\}_{jk} = \int_{S_k} \partial_{yy}^2 G\left(\mathbf{r}, \mathbf{r}'\right)\big|_{\mathbf{r}=\mathbf{r}_j} ds'.$$

Similarly, inserting (4) into (3) yields a system of equations:

$$\bar{E}^{sca} = \bar{H} D(\bar{E}) \bar{P} \bar{t}. \tag{7}$$

Here, $\bar{E}^{sca}$ is a $3N \times 1$ vector, and $\bar{P}$ and $\bar{H}$ are $3N \times N$ and $3N^R \times 3N$ matrices, respectively, which are expressed in terms of other vectors and matrices as

$$\bar{E}^{sca} = \begin{bmatrix} \bar{E}_x^{sca} \\ \bar{E}_y^{sca} \\ \bar{E}_z^{sca} \end{bmatrix}, \quad P = \begin{bmatrix} \bar{I} \\ \bar{I} \\ \bar{I} \end{bmatrix}, \quad \bar{H} = \begin{bmatrix} -\bar{G}_{yy}^R & \bar{G}_{xy}^R & 0 \\ \bar{G}_{xy}^R & -\bar{G}_{xx}^R & 0 \\ 0 & 0 & -k_0^2 \bar{G}^R \end{bmatrix}. \tag{8}$$

In (8), $\bar{E}_u^{sca}$ are $N \times 1$ vectors storing samples of $E_u^{sca}(\mathbf{r})$ at $\mathbf{r}_m^R$, i.e., $\{\bar{E}_u^{sca}\}_m = E_u^{sca}(\mathbf{r}_m^R)$, $m = 1, \ldots, N^R$, and $\bar{G}^R$, $\bar{G}_{xx}^R$, $\bar{G}_{xy}^R$, and $\bar{G}_{yy}^R$ are $N \times N$ matrices storing the samples of the convolution between $p_k(\mathbf{r}')$ and $G(\mathbf{r}, \mathbf{r}')$, $\partial_{xx}^2 G(\mathbf{r}, \mathbf{r}')$, $\partial_{xy}^2 G(\mathbf{r}, \mathbf{r}')$, and $\partial_{yy}^2 G(\mathbf{r}, \mathbf{r}')$, i.e.,

$$\begin{aligned}
\{\bar{G}^R\}_{mk} &= \int_{S_k} G\left(\mathbf{r}_m^R, \mathbf{r}'\right) ds', \\
\{\bar{G}_{xx}^R\}_{mk} &= \int_{S_k} \partial_{xx}^2 G\left(\mathbf{r}, \mathbf{r}'\right)\big|_{\mathbf{r}=\mathbf{r}_m^R} ds', \\
\{\bar{G}_{xy}^R\}_{mk} &= \int_{S_k} \partial_{xy}^2 G\left(\mathbf{r}, \mathbf{r}'\right)\big|_{\mathbf{r}=\mathbf{r}_m^R} ds', \\
\{\bar{G}_{yy}^R\}_{mk} &= \int_{S_k} \partial_{yy}^2 G\left(\mathbf{r}, \mathbf{r}'\right)\big|_{\mathbf{r}=\mathbf{r}_m^R} ds'.
\end{aligned}$$

The relation between $\bar{E}^{sca}$ and $\bar{t}$, i.e., the forward solver, is obtained by inserting $\bar{E} = \bar{F}^{-1} \bar{E}^{inc}$ from (5) into (7):

$$\bar{E}^{sca} = \bar{H} D\left(\bar{F}^{-1} \bar{E}^{inc}\right) \bar{P} \bar{t} = f\left(\bar{t}\right). \tag{9}$$

It is clear from (6) that $\bar{F}^{-1}$ is a function of $\bar{t}$. Consequently, the forward operator $f(\bar{t})$ defines a nonlinear function in $\bar{t}$. The "decoupled" $2N \times 2N$ and $N \times N$ matrix blocks in $\bar{F}$ and $\bar{F}^{-1}$, and $2N^R \times 2N$ and $N^R \times N$ matrix blocks in $\bar{H}$ indicate that $f(\bar{t})$ can be separated into TM ($u \in \{x, y\}$) and TE ($u = z$) components, each of which can be accounted for individually [see (6) and (8)]. This is implicitly assumed in the rest of the text. Additionally, $f(\bar{t})$ in (9) is derived assuming that there is only one transmitter. In the case of multiple transmitters, each of which is used individually for generating a separate $\bar{E}^{inc}$, $f(\bar{t})$ is obtained by cascading the matrices in (9) for each of the transmitters. One can also account for changes in receiver locations (from one excitation to another) by re-computing the matrix $\bar{H}$ before the cascade operation.

2.3. Nonlinear Sparse Optimization

Let $\bar{E}_u^{mea}$, $u \in \{x, y, z\}$ represent $N \times 1$ vectors storing samples of the components of the scattered electric field *measured* at $\mathbf{r}_m^R$, i.e., $\{\bar{E}_u^{mea}\}_m = E_u^{mea}(\mathbf{r}_m^R)$, $m = 1, \ldots, N^R$. Also, let $\bar{E}^{mea}$ represent the $3N \times 1$ vector obtained by cascading $\bar{E}_u^{mea}$:

$$\bar{E}^{mea} = \begin{bmatrix} \bar{E}_x^{mea} \\ \bar{E}_y^{mea} \\ \bar{E}_z^{mea} \end{bmatrix}. \tag{10}$$

Using these definitions, the "discretized" inverse problem is constructed as finding $\bar{t}$ by minimizing the data misfit between $\bar{E}^{mea}$ and $\bar{E}^{sca}$, which is expressed as a nonlinear function of $\bar{t}$ using the forward operator in (9). The discretized inverse problem also suffers from ill-conditioning like its continuous counterpart as described in Section 2.1. The effects of ill-conditioning can be alleviated by constraining the minimization problem with a penalty term as [2, 3]:

$$\bar{t} = \arg\min_{\bar{t}} \frac{1}{2} \left\| f(\bar{t}) - \bar{E}^{mea} \right\|_2^2 + \gamma \left\| \bar{t} \right\|_l. \tag{11}$$

The first term in (11) is the least-squares data misfit between $\bar{E}^{mea}$ and $\bar{E}^{sca} = f(\bar{t})$, and the second term $\|\bar{t}\|_l$ is the penalty. The regularization parameter γ is a measure of the "trade off" between the data misfit and penalty term. The norm used in the penalty terms changes the characteristics of the regularized solution. Sparsity is promoted by choosing $l = 0$ (zeroth norm) or $l = 1$ (first norm) [3, 32]. It should be emphasized here that the sparsity constraint is enforced directly in the spatial domain where the unknown contrast $\tau(\mathbf{r})$ resides, i.e., it is assumed that many entries of $\bar{t}$, which stores the coefficients of spatial basis expansion of $\tau(\mathbf{r})$, are zero. If this condition is not satisfied, one can apply a transformation, such wavelet or discrete cosine transform, to obtain a "sparsified" basis expansion of $\tau(\mathbf{r})$.

The minimization in (11) is carried out using thresholded nonlinear Landweber (NLW) iterations as described next. These iterations read

Step 1) select $\gamma, \bar{t}_{(1)}$
Step 2) for $i = 1, 2, \ldots, N^{LW}$
Step 3) $\quad \bar{r}_{(i)} = \bar{E}^{mea} - f\left(\bar{t}_{(i)}\right)$
Step 4) $\quad \bar{t}_{(i+1)} = T_l^{\gamma}\left(\bar{t}_{(i)} + \beta_{(i)}\, \partial_t f^*|_{\bar{t}=\bar{t}_{(i)}}\left(\bar{r}_{(i)}\right)\right)$
Step 5) end

In the above algorithm, subscript (i) attached to a variable indicates that the variable belongs to the ith NLW iteration. Step 1 of the algorithm is the initialization, where the values of γ and $\bar{t}_1$ are set. In most problems, choosing $\bar{t}_1 = 0$ gives convergent results. Value of γ is determined heuristically based on the levels of noise in $\bar{E}^{mea}$, numerical modeling error, and ill-conditioning of the problem, which depends on the electrical size of S and numbers of receivers and transmitters. At Step 4, operator $\partial_{\bar{t}} f^*(\bar{t})$ is the adjoint of the operator $\partial_{\bar{t}} f(\bar{t})$, which is the Frechet derivative of the nonlinear function $f(\bar{t})$. Operator $\partial_{\bar{t}} f(\bar{t})$ is obtained from (9) as [25]:

$$\partial_{\bar{t}} f\left(\bar{t}\right) = \bar{H}\bar{M}^{-1} D\left(\bar{F}^{-1}\bar{E}^{inc}\right) \tag{12}$$

where matrices $\bar{F}$ and $\bar{H}$ are given in (6) and (8), respectively, while $\bar{M}$ is expressed as

$$\bar{M} = \begin{bmatrix} \bar{I} + D\left(\bar{t}\right)\left(\bar{I} + \bar{G}_{yy}\right) & -D\left(\bar{t}\right)\bar{G}_{xy} & 0 \\ -D\left(\bar{t}\right)\bar{G}_{xy} & \bar{I} + D\left(\bar{t}\right)\left(\bar{I} + \bar{G}_{xx}\right) & 0 \\ 0 & 0 & \bar{I} + k_0^2 D\left(\bar{t}\right)\bar{G} \end{bmatrix}.$$

At Step 4, $\beta_{(i)}$ is the step size of the ith NLW iteration. To ensure convergence, it is selected as $\beta_{(i)} = 1/\sigma_{(i)}^2$, where $\sigma_{(i)}$ is the maximum singular value of the matrix/operator $\partial_{\bar{t}} f(\bar{t})|_{\bar{t}=\bar{t}_{(i)}}$ [32]. It should be noted here that an accurate approximation to $\sigma_{(i)}$ is computed very efficiently with only a few steps of power iterations. Additionally, $\sigma_{(i)}$ does not change significantly as the NLW iterations evolve. Therefore $\beta_{(i)}$ is estimated only every few iterations to prevent extra computational work.

The sparsity constraint in the minimization problem (11) is enforced within the NLW iterations by applying the thresholding function $T_l^{\gamma}(\cdot)$ as shown in Step 4 of the above algorithm. If the penalty term is the zeroth norm ($l = 0$), then $T_0^{\gamma}(\cdot)$ is known as hard-thresholding and is defined in complex domain as [38]

$$\left\{T_0^{\gamma}\left(\{\bar{t}\}_k\right)\right\}_k = \begin{cases} \{\bar{t}\}_k, & \text{if } \left|\{\bar{t}\}_k\right| > \sqrt{2\gamma} \\ 0, & \text{otherwise} \end{cases}, \quad k = 1, \ldots, N.$$

If the penalty term is the first norm ($l = 1$), then $T_1^{\gamma}(\cdot)$ is known as soft-thresholding and is defined in complex domain as [39]

$$\left\{T_1^{\gamma}\left(\{\bar{t}\}_k\right)\right\}_k = \frac{\max\left[\left|\{\bar{t}\}_k\right| - \gamma, 0\right]}{\max\left[\left|\{\bar{t}\}_{(k)}\right| - \gamma, 0\right] + \gamma}\{\bar{t}\}_k, \quad k = 1, \ldots, N.$$

The NLW iterations are truncated when a stopping criterion based on the discrepancy principle [40]

$$\left\|\bar{r}_{(i)}\right\| \leq \delta$$

is satisfied. Here, δ is a user-defined tolerance chosen based on the levels of noise in $\bar{E}^{mea}$, numerical modeling error, and ill-conditioning of the problem [3, 19]. This stopping criterion can also be implemented by simply setting the maximum number of iterations N^{LW} to a fixed number, which is determined heuristically like the tolerance δ.

It should be mentioned here that truncating NLW iterations (by setting N^{LW} to a fixed number) is a regularization in itself. NLW iterations "recover" the components of the solution with smaller variations first and proceed to the components with larger variations. Consequently, truncation of the NLW iterations eliminates the higher-frequency components, which are more susceptible to noise and possibly corrupted in the presence of high levels of noise and numerical modeling error. This regularizes the solution by promoting smoothness. Following the discussion above, if one replaces Step 4 with

$$\bar{t}_{(i+1)} = \bar{t}_{(i)} + \beta_{(i)}\, \partial_t f^*|_{\bar{t}=\bar{t}_{(i)}} \left(\bar{r}_{(i)}\right)$$

i.e., eliminates the thresholding, the resulting truncated (but not thresholded) NLW iterations will lead to a smooth solution; and in essence this is equivalent choosing $l = 2$ in the minimization problem (11).

The computational cost of the NLW iterations is dominated by the cost of matrix inversions required at Steps 3 and 4. More specifically, at the ith iteration, matrices $\bar{F}$ [see (9)] and $\bar{M}$ [see (12)] are inverted to compute $f(\bar{t}_{(i)})$ and $\partial_t f^*|_{\bar{t}=\bar{t}_{(i)}} \left(\bar{r}_{(i)}\right)$. These matrix inversions are carried out iteratively using the stabilized bi-conjugate gradient (STABICG) method. At every iteration of the STABICG method, matrix $\bar{F}$ or $\bar{M}$ is multiplied by a vector. This matrix-vector multiplication is carried out very efficiently with $O(N \log N)$ computational cost using FFTs since $\bar{G}$, $\bar{G}_{xx}$, $\bar{G}_{yy}$, and $\bar{G}_{xy}$ are all Toeplitz matrices [37]. Additionally, only one column of each of these matrices is needed in the FFT-accelerated matrix-vector multiplication. The computational cost of computing and memory requirement of storing this one column scale as $O(N)$ [37]. This operation is done only once before the NLW iterations start. It should also be mentioned here that the the computational complexity of the NLW iterations stay the same when they are applied to three-dimensional (3-D) domains. But in this case, N scales as $(D/\Delta d)^3$, where D and Δd are dimensions of the domain and the cell where the pulse basis function is defined. As with any other inversion algorithm, this makes the computational cost of solving 3-D problems significantly higher than that of solving 2-D problems.

2.4. Frequency Hopping

Oftentimes, in microwave imaging problems, the measurements are taken at multiple frequencies. If $\tau(\mathbf{r})$ does not depend on frequency, the algorithm described in the previous section can still be used for sparsity-constrained inversion after $\partial_{\bar{t}} f(\bar{t})$ is constructed by cascading matrices $\bar{H}$, $\bar{M}^{-1}$, and $\bar{F}^{-1}$ computed for every frequency. This approach makes the NLW iterations more susceptible to converging to a local minimum [of the minimization problem (11)] far from the actual solution especially if the nonlinearity is strong. Also, it obviously cannot be used if $\tau(\mathbf{r})$ depends on frequency. An alternative approach that does not suffer from these drawbacks is proposed in this section.

Let $\tau(\mathbf{r}) = \chi(\mathbf{r}) - j\sigma(\mathbf{r})/(\omega\varepsilon_0)$ represent the frequency dependent contrast function. Here, $\chi(\mathbf{r})$ and $\sigma(\mathbf{r})$ are the susceptibility and the conductivity on S. Define $\bar{\chi}$ and $\bar{\sigma}$ as $N \times 1$ vectors storing samples of $\chi(\mathbf{r})$ and $\sigma(\mathbf{r})$ on S, i.e., $\{\bar{\chi}\}_k = \chi(\mathbf{r}_k)$ and $\{\bar{\sigma}\}_k = \sigma(\mathbf{r}_k)$, $k = 1, \ldots, N$. In the case of multiple frequency measurements, the algorithm describing NLW iterations given in the previous section is updated as

Step 1) select $\gamma^{(1)}, \bar{\chi}^{(0)}, \bar{\sigma}^{(0)}$
Step 2) for $p = 1, 2, \ldots, N^{FRE}$
Step 3) $\quad \bar{t}_{(i)} = \bar{\chi}^{(p-1)} - j\bar{\sigma}^{(p-1)} / \left(\omega^{(p)}\varepsilon_0\right)$
Step 4) $\quad$ for $i = 1, 2...., N^{LW}$
Step 5) $\quad\quad \bar{r}_{(i)} = \bar{E}^{mea} - f\left(\bar{t}_{(i)}\right)$
Step 6) $\quad\quad \bar{t}_{(i+1)} = T_l^{\gamma^{(p)}} \left(\bar{t}_{(i)} + \beta_{(i)}\, \partial_t f^*|_{\bar{t}=\bar{t}_{(i)}} \left(\bar{r}_{(i)}\right)\right)$
Step 7) $\quad$ end
Step 8) $\quad \bar{\chi}^{(p)} = \mathrm{Re}\left\{\bar{t}_{(i+1)}\right\}, \bar{\sigma}^{(p)} = -\left(\omega^{(p)}\varepsilon_0\right) \mathrm{Im}\left\{\bar{t}_{(i+1)}\right\}$
Step 9) end

In the above frequency-hopping algorithm, superscript (p) indicates that the variable it is attached to belongs to the pth frequency step. At Step 1 $\bar{\chi}^{(0)}$ and $\bar{\sigma}^{(0)}$ are initialized to zero and $\bar{t}_{(i)}$ computed at Step 3 serves as an initial guess for NLW iterations applied at the next frequency step. Steps 4 to 7 are the thresholded-NLW iterations running over a single frequency as described before. Step 8 retrieves $\bar{\chi}^{(p)}$ and $\bar{\sigma}^{(p)}$ from $\bar{t}_{(i+1)}$ to initialize the NLW iterations at the next frequency step. This procedure accelerates the convergence of the NLW iterations by "steering them away" from a possible local minimum.

3. NUMERICAL RESULTS

In this section, the accuracy, efficiency, and applicability of the proposed method are demonstrated via several examples, where domains of different electric sizes, contrast, and sparseness levels are investigated under different excitations. In all examples, $\bar{E}^{mea}$ is obtained from actual measurements or synthetically generated as described next. Let $\tau^{ref}(\mathbf{r})$ and $\bar{t}^{ref}$ represent the actual (known) contrast and the vector that stores its samples. $\bar{t}^{ref}$ is inserted in (5); let the solution of the resulting system be represented with $\bar{E}^{ref}$. Then, $\bar{t}^{ref}$ and $\bar{E}^{ref}$ are used in (7) to yield $\bar{E}^{s,ref}$. Finally $\bar{E}^{mea}$ is generated by adding white Gaussian noise to $\bar{E}^{s,ref}$. The level of this noise is measured in decibels using $20\log_{10}(\text{SNR})$, where SNR is the signal to noise ratio.

In all examples, unless stated otherwise, the results are obtained using two methods (i) Thresholded and truncated NLW iterations (termed as sparsity promoting NLW iterations and abbreviated as SP-NLW) and (ii) truncated NLW iterations (termed as smoothness promoting NLW iterations and abbreviated as SM-NLW). The relative norm error in (complex) contrast samples recovered at the ith NLW iteration is computed using

$$err^{(i)} = \sqrt{\frac{\sum_{n=1}^{N}\left|\{\bar{t}_i\}_n - \{\bar{t}^{\text{ref}}\}_n\right|^2}{\sum_{n=1}^{N}\left|\{\bar{t}^{\text{ref}}\}_n\right|^2}}.$$

It should be noted here that if only the amplitude of the scattered fields are measured at $\mathbf{r}_m^R$, $m = 1, \ldots, N^R$, a phase retrieval technique [1] has to be applied to compute the complex values of $\bar{E}^{mea}$. Then, the proposed method can be used on those values. Another option is to modify the proposed method so that it minimizes the difference between the amplitudes of $\bar{E}^{mea}$ and $\bar{E}^{sca}$, i.e., optimizes a phaseless functional [1]. One might expect that this modification will deteriorate the efficiency and/or accuracy of the method. But it is safe to say that this is also expected from existing schemes extended to invert phaseless scattered field data [1].

3.1. Circular Ring Scatterer

The relative permittivity profile of the domain and the transmitter-receiver configuration are shown in Figure 2(a). The relative permittivities of the inner circle and outer ring are 2 and 2.5, respectively. The investigation domain is discretized using $N = 2500$ square cells with dimension $\Delta d = 0.15\,\text{m}$. The sparseness level in $\bar{t}^{ref}$ is 3.4%. The numbers of transmitters and receivers are $N^R = 52$ and $N^T = 12$, respectively. The frequency of the transmitters is $f = 125\,\text{MHz}$. The level of noise in synthetically generated $\bar{E}^{mea}$ is 25 dB. $N^{LW} = 200$ for both SP-NLWs and SM-NLW, and $\gamma = 0.01$ and $\gamma = 0.09$ for soft- and hard-thresholded SP-NLWs.

Figure 2(b) plots $err^{(i)}$ computed by the soft/hard-thresholded SP-NLWs and the SM-NLW. At iteration $i = 200$, $err^{(i)}$ reaches 45.6%, 54.9%, and 77.3%, for the soft/hard-thresholded SP-NLWs and the SM-NLW, respectively. The figure shows faster convergence for the SP-NLWs over the SM-NLW. Relative permittivity profiles recovered at iteration $i = 200$ by the three methods are shown in Figures 2(c), 2(d), and 2(e), respectively. In Figures 2(c) and 2(d) the inner circle and the outer ring are well separated but in Figure 2(e) they are detected as one object. These figures clearly demonstrate the benefits of the sparsity constrained regularization.

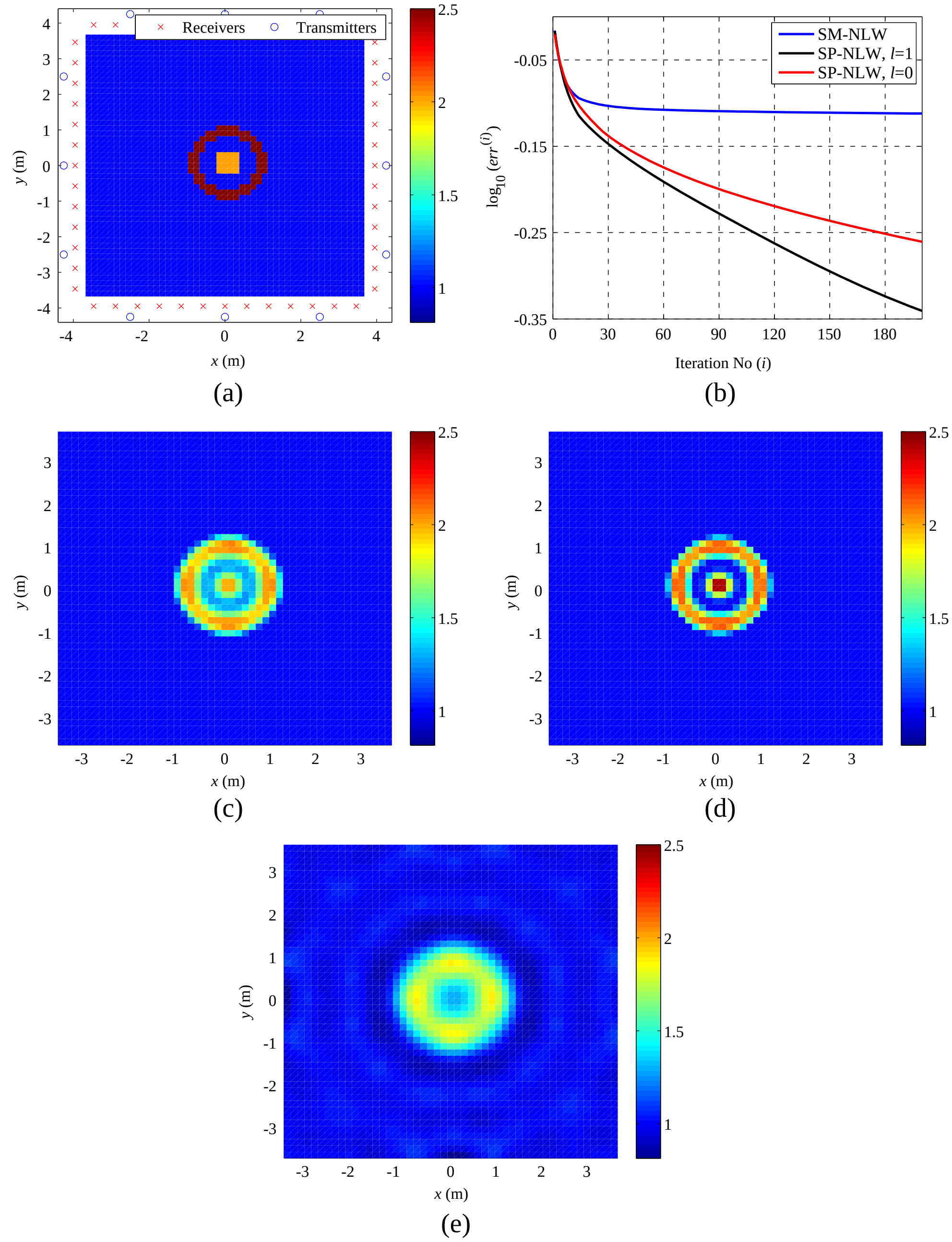

Figure 2. Circular ring scatterer. (a) Actual relative permittivity profile and locations of the transmitters and receivers. (b) $err^{(i)}$ computed by hard-thresholded ($l = 0$) and soft-thresholded ($l = 1$) SP-NLW and SM-NLW. Permittivity profiles recovered at $i = 200$ by (c) SP-NLW with $l = 1$ (d) SP-NLW with $l = 0$, and (e) SM-NLW.

3.2. Austria Scatterer

The well-known Austria scatterer [29] is considered in this example. The relative permittivity profile of the domain and the transmitter-receiver configuration are shown in Figure 3(a). The relative permittivities of the small circles and large ring are 2.5 and 2, respectively. The investigation domain is discretized using $N = 2500$ square cells with dimension $\Delta d = 0.15\,\mathrm{m}$. The sparseness level in $\bar{t}^{ref}$ is 11.5%. The numbers of transmitters and receivers are $N^R = 32$ and $N^T = 8$, respectively. The frequency of the transmitters is $f = 125\,\mathrm{MHz}$. Three different noise levels are considered: 25 dB, 10 dB,

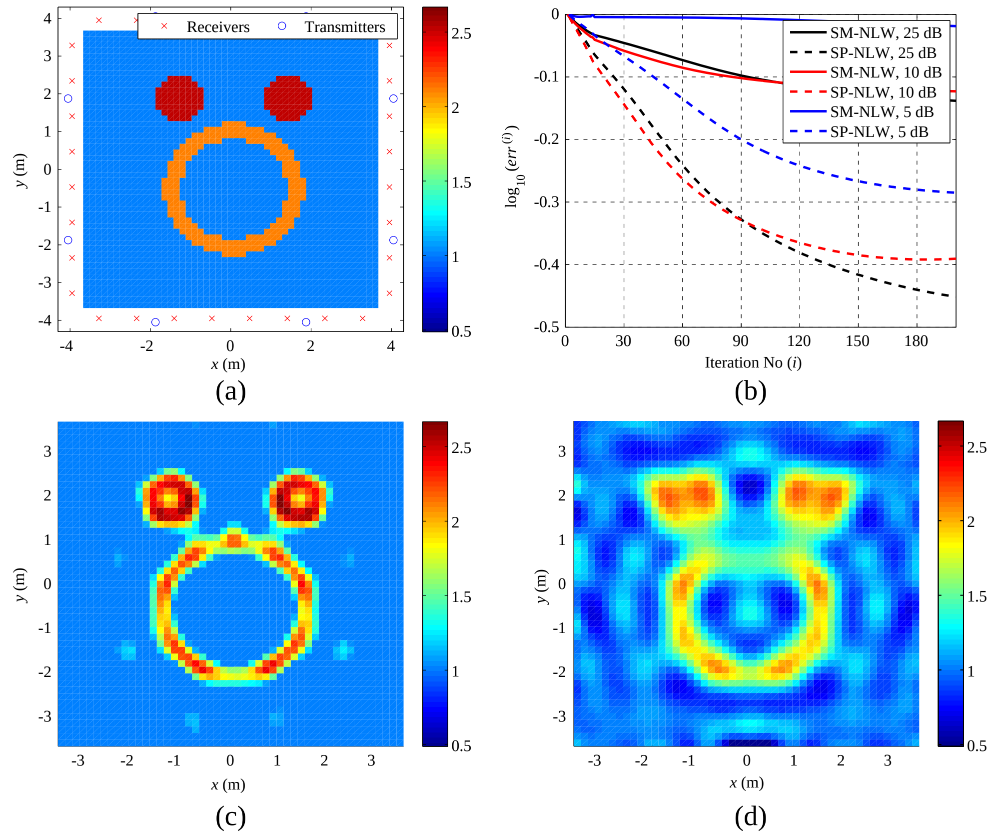

Figure 3. Austria scatterer. (a) Actual relative permittivity profile and locations of the transmitters and receivers. (b) $err^{(i)}$ computed by soft-thresholded ($l = 1$) SP-NLW and SM-NLW for different noise levels. Permittivity profiles recovered at $i = 200$ by (c) SP-NLW with $l = 1$ and SM-NLW for 25 dB noise.

and 5 dB noise is added to synthetically generated $\bar{E}^{mea}$. $N^{LW} = 200$ for the soft-thresholded SP-NLW and the SM-NLW, and $\gamma = 0.01$ for the SP-NLW.

Figure 3(b) plots $err^{(i)}$ computed by the SP-NLW and the SM-NLW for all three levels of noise. At iteration $i = 200$, for $\bar{E}^{mea}$ generated with 25 dB, 10 dB, and 5 dB noise, $err^{(i)}$ computed by the SM-NLW reaches 72.8%, 75%, and 95.75%, respectively, while for the SP-NLW it reaches 35.4%, 38.61%, and 51.89%, respectively. This figure clearly illustrates that the SP-NLW is significantly more immune to noise than the SM-NLW for this example. Figures 3(c) and 3(d) provide the relative permittivity profiles recovered by the SP-NLW and the SM-NLW at iteration $i = 200$ for $\bar{E}^{mea}$ generated with 25 dB noise, respectively. The profile recovered under sparsity-constrained regularization is clearly more accurate and sharper.

3.3. Layered Circular Scatterer

The relative permittivity profile of the domain and the transmitter-receiver configuration are shown in Figure 4(a). The relative permittivities of the smaller and outer larger circles are 1.5 and 2.5, respectively. The investigation domain is discretized using $N = 2500$ square cells with dimension $\Delta d = 0.15$ m. The sparseness level in $\bar{t}^{ref}$ is 9.9%. The numbers of transmitters and receivers are $N^R = 32$ and $N^T = 8$, respectively. The frequency of the transmitters is $f = 125$ MHz. The level of noise in synthetically generated $\bar{E}^{mea}$ is 25 dB. $N^{LW} = 200$ for the soft-thresholded SP-NLW and the SM-NLW, and $\gamma = 0.008$ for the SP-NLW.

Figure 4(b) plots $err^{(i)}$ computed by the SP-NLW and the SM-NLW. At iteration $i = 200$, $err^{(i)}$

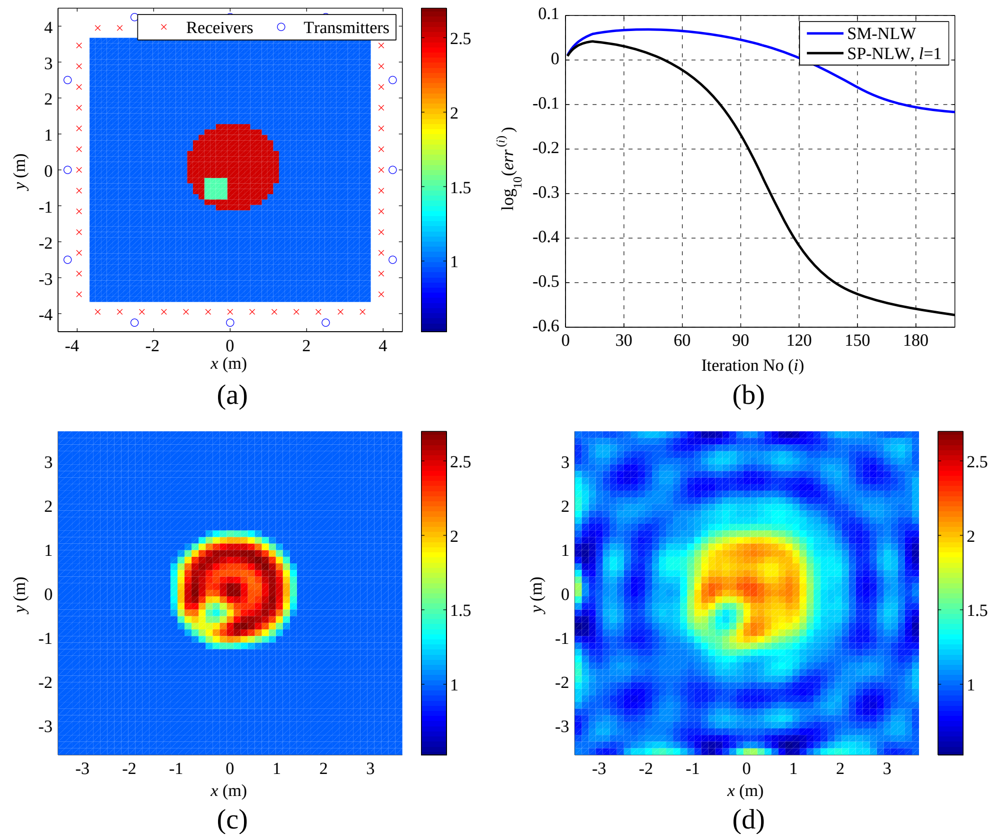

Figure 4. Layered circular scatterer. (a) Actual relative permittivity profile and locations of the transmitters and receivers. (b) $err^{(i)}$ computed by soft-thresholded ($l = 1$) SP-NLW and SM-NLW. Permittivity profiles recovered at $i = 200$ by (c) SP-NLW with $l = 1$ and (d) SM-NLW.

reaches 26.8% and 74.6% for the SP-NLW and the SM-NLW, respectively. Figures 4(c) and 4(d) provide the relative permittivity profiles recovered by the SP-NLW and the SM-NLW at iteration $i = 200$, respectively. In the profile recovered by the SP-NLW, the two circles are more clearly identified.

3.4. Layered Square Scatterer

The susceptibility and conductivity profiles of the domain together with the transmitter-receiver configuration are shown in Figures 5(a) and 5(b), respectively. The susceptibilities and conductivities of the smaller and outer larger squares are $\{10,\ 3\,\mathrm{mS/m}\}$ and $\{6,\ 3\,\mathrm{mS/m}\}$, respectively. The investigation domain is discretized using $N = 3025$ square cells with dimension $\Delta d = 0.15\,\mathrm{m}$. The sparseness level in $\bar{t}^{ref}$ is 14.58%. The numbers of transmitters and receivers are $N^R = 32$ and $N^T = 8$, respectively. The transmitters are operated two frequencies: 10 MHz and 40 MHz. $N^{LW} = 75$ for the soft-thresholded SP-NLW and SM-NLW, and $\gamma^{(1)} = 0.01, \gamma^{(2)} = 0.001$ for the SP-NLW.

Figure 5(c) plots $err^{(i)}$ computed by the SP-NLW and the SM-NLW at frequency steps $p = 1$ and $p = 2$. At iteration $i = 75$ and the frequency step $p = 2$, $err^{(i)}$ reaches 26.7% and 50.7% for the SP-NLW and the SM-NLW, respectively. Figures 5(d) and 5(e) provide the susceptibility profiles recovered by the SP-NLW and the SM-NLW at iteration $i = 75$ and the frequency step $p = 2$, respectively. Similarly, Figures 5(f) and 5(g) provide the recovered conductivity profiles. The SP-NLW is more accurate; the profile recovered by the SM-NLW resembles a circle more than square. Furthermore, the layer interface is more distinguishable in profiles recovered by the SP-NLW.

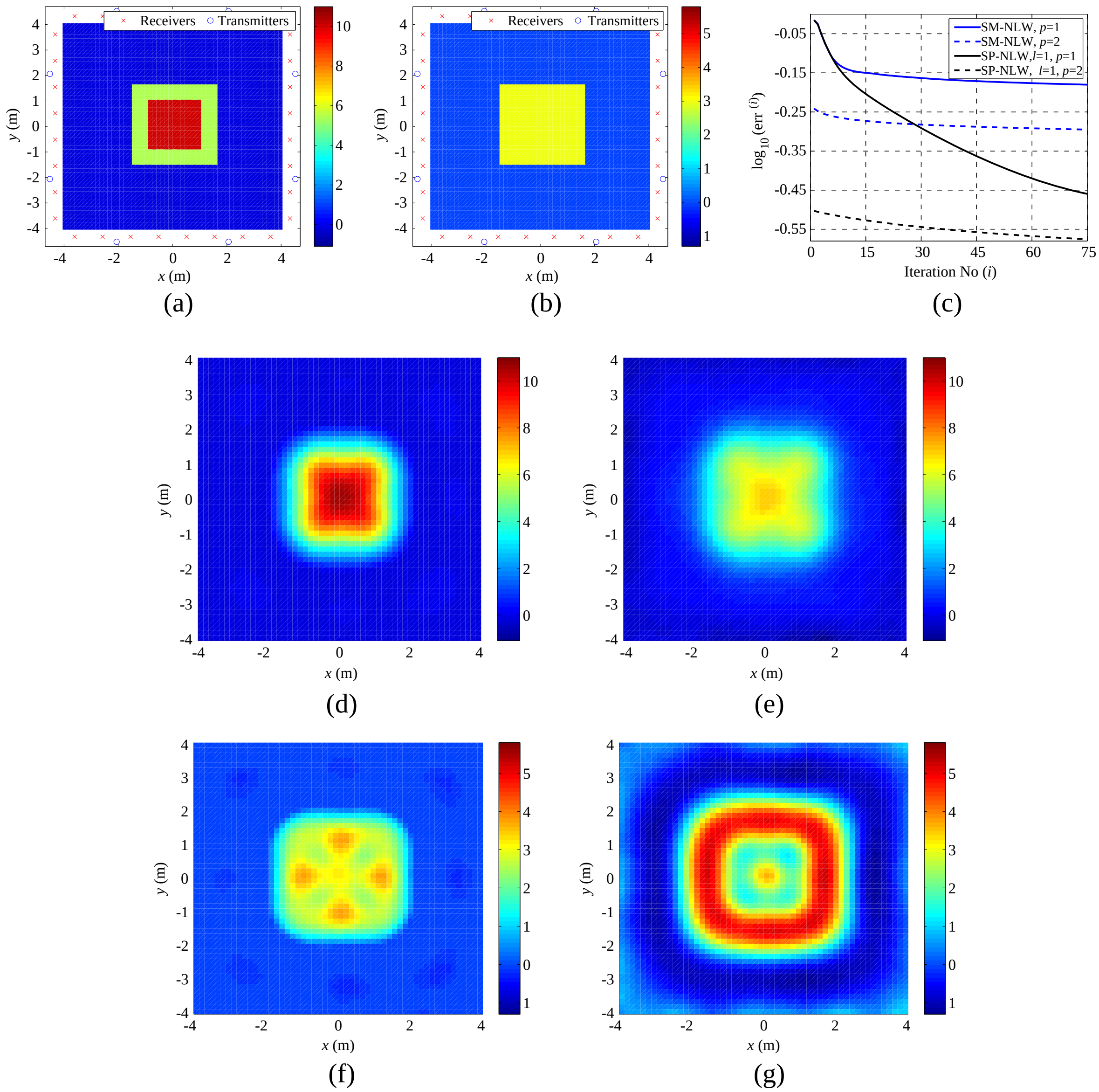

Figure 5. Layered square scatterer. Locations of transmitters and receivers and actual (a) susceptibility and (b) conductivity profiles. (c) $err^{(i)}$ computed by soft-thresholded ($l = 1$) SP-NLW and SM-NLW for frequency steps $p = 1$ and $p = 2$. (d) Susceptibility profiles recovered at $i = 75$ by (d) SP-NLW with $l = 1$ and (e) SM-NLW. Conductivity profiles recovered at $i = 75$ by (f) SP-NLW with $l = 1$ and (g) SM-NLW.

3.5. Two Circular Scatterers

The relative permittivity profile of the domain is shown in Figure 6(a). The relative permittivities of the plastic scatterer (smaller circle with radius 31 mm) and the foam scatterer (larger circle with radius 80 mm) are 3 ± 0.3 and 1.45 ± 0.15, respectively. The investigation domain is discretized using $N = 2500$ square cells with dimension $\Delta d = 4.4$ mm. The sparseness level in $\bar{t}^{ref}$ is 9.92%. The receiver-transmitter configuration is described in [41] and the transmitters are operated at frequency $f = 2$ GHz. Samples $\bar{E}^{mea}$ are generated from actual measurement field values provided in "FoamDielExtTE" and "FoamDielExtTM" by [41]. Additionally, the calibration process described in [42] is used to generate the incident field in the investigation domain. $N^{LW} = 200$ for the soft-thresholded SP-NLW and the

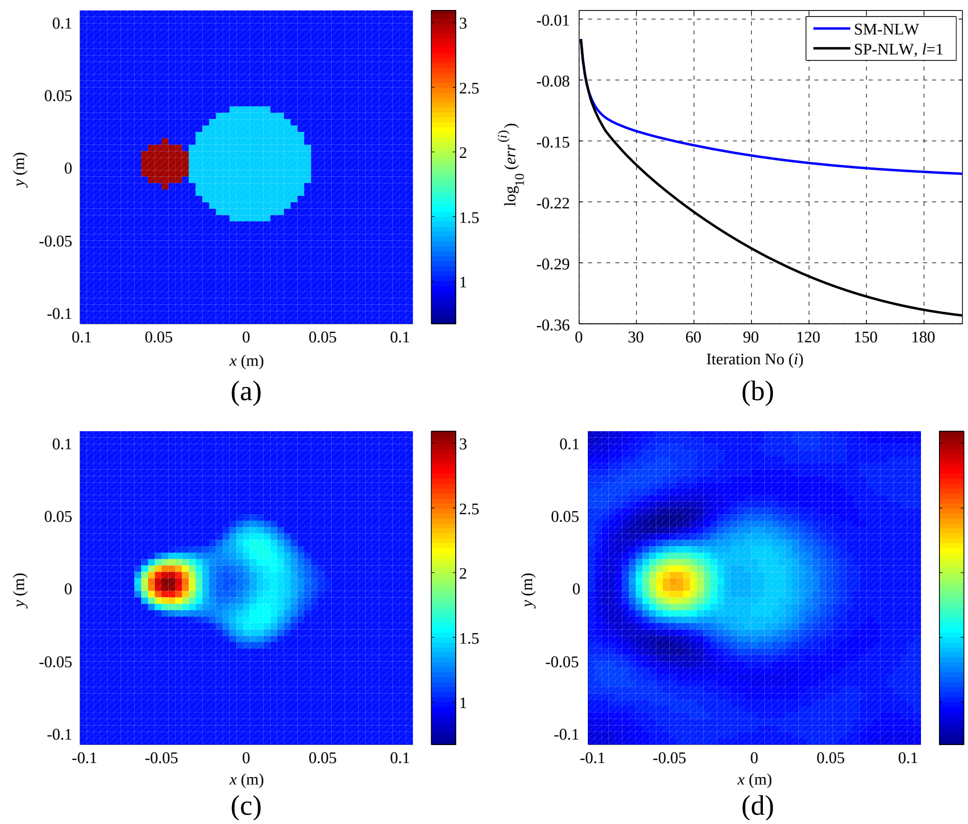

Figure 6. Two circular scatterers. (a) Actual relative permittivity profile. (b) $err^{(i)}$ computed by soft-thresholded ($l = 1$) SP-NLW and SM-NLW. Permittivity profiles recovered at $i = 200$ by (c) SP-NLW with $l = 1$ and (d) SM-NLW.

SM-NLW, and $\gamma = 0.009$ for the SP-NLW.

Figure 6(b) plots $err^{(i)}$ computed by the SP-NLW and the SM-NLW. At iteration $i = 200$, $err^{(i)}$ reaches 44.7% and 64.9% for the SP-NLW and the SM-NLW, respectively. The relative permittivity profiles recovered at iteration $i = 200$ by the two methods are shown in Figures 6(c) and 6(d). The SP-NLW is more accurate in predicting the levels of the actual permittivity.

3.6. Range of Validity

In the last example, the applicability of the SP-NLW to investigation domains involving strong scatterers with high values of permittivity is demonstrated. The investigation domain, the locations of the transmitters and the receivers, and the discretization parameters are same as those described in Section 3.2. Four scenarios, where the relative permittivity of the ring and eyes is set to 1.8, 2.0, 2.2, and 2.4, are considered. The transmitters are operated at four frequencies: 129 MHz, 134 MHz, 140 MHz, and 150 MHz for all scenarios. The level of noise in synthetically generated $\bar{E}^{mea}$ is 25 dB. The results obtained by the soft-thresholded SP-NLW are compared to those obtained by the soft-thresholded Born iterative method (SP-BIM) described in [19]. For the SP-BIM, the inner thresholding loop, which enforces the sparsity constraint, is truncated at $N_{it}^{REG} = 3$ iterations for the first five Born iterations, then at $N_{it}^{REG} = 5$ up to the tenth Born iteration, and, finally, at $N_{it}^{REG} = 10$ until the Born iterations are completed. For both the SP-NLW and the SP-BIM $\gamma = 0.01$.

Figures 7(a) and 7(b) plot $err^{(i)}$ computed by the SP-BIM and the SP-NLW vs. the execution time required for the ith iteration to be completed, for all four scenarios considered. Note that here i stands for either the LW or BIM iterations. Figures clearly show that the SP-BIM fails to converge when the relative permittivity of the scatterer is increased to 2.0, 2.2, or 2.4 while the SP-NLW recovers

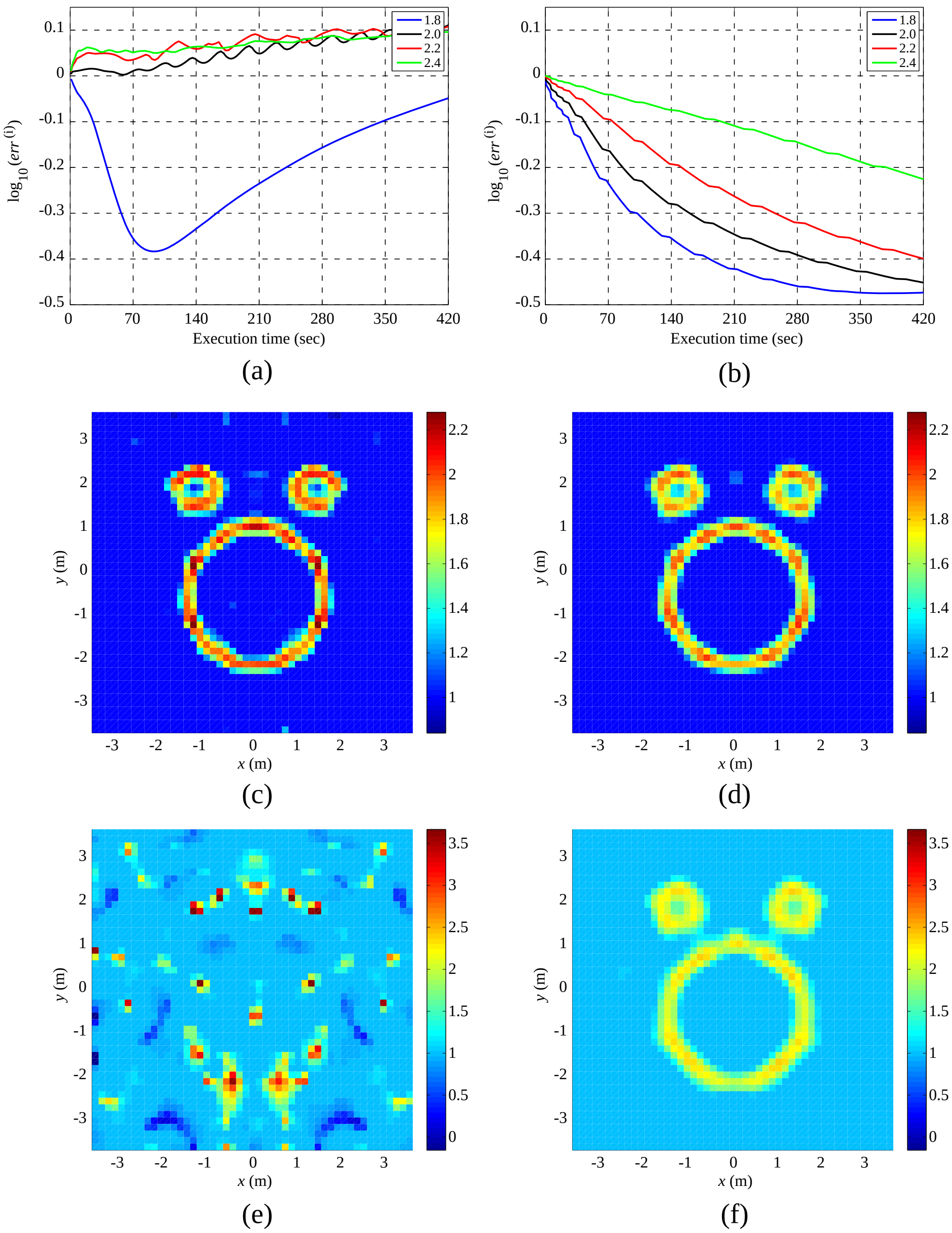

Figure 7. Four Austria scatterers with relative permittivities 1.8, 2.0, 2.2, and 2.4. $err^{(i)}$ computed by (a) the soft-thresholded SP-BIM [19] and (b) the soft-thresholded SP-NLW. The relative permittivity profiles recovered by (c) the SP-BIM at iteration $i = 50$ and (d) the SP-NLW at iteration $i = 155$ for the scatterer with relative permittivity 1.8. The relative permittivity profiles recovered by (e) the SP-BIM and (f) the SP-NLW at iteration $i = 200$ for the scatterer with relative permittivity 2.2.

the investigation domain accurately even when the relative permittivity of the scatterer is as high as 2.4.

For the scenario with the weakest scatterer with relative permittivity 1.8, the SP-BIM achieves the lowest error $err^{(50)} = 43.66\%$ at iteration $i = 50$. Figure 7(c) shows the relative permittivity profile recovered by the SP-BIM at iteration $i = 50$. For the same scenario, the SP-NLW achieves the lowest error $err^{(155)} = 33.42\%$ at iteration $i = 155$. Figure 7(d) shows the relative permittivity profile recovered by the SP-NLW at iteration $i = 155$. Higher accuracy obtained by the SP-NLW comes at the cost of approximately fivefold increase in the execution time. This is expected since it is well-known that the BIM is rather efficient in recovering investigation domains involving weak scatterers.

On the other hand, a comparison of the profiles, for the scatterer with relative permittivity 2.2, recovered by the SP-BIM at iteration $i = 200$ ($err^{(200)} = 102.1\%$) and the SP-NLW at iteration $i = 200$ ($err^{(200)} = 35.31\%$), which are respectively shown in Figures 7(e) and 7(f), clearly demonstrates the benefits of the SP-NLW. The profile recovered by the SP-NLW is accurate while that obtained by the SP-BIM shows a clearly-diverged solution.

4. CONCLUSION

Thresholded and truncated NLW iterations are used to efficiently and accurately solve the 2-D electromagnetic inverse scattering problem that is constructed as least squares data misfit between the scattered and measured fields, which are expressed as a nonlinear function of the permittivity and the measured fields. Thresholding enforces the sparseness-promoting L_0/L_1 norm penalty term on the data misfit. Numerical results demonstrate that the permittivity profiles reconstructed using thresholded and truncated NLW iterations are sharper and more accurate than those obtained by only truncated NLW iterations, especially when applied to sparse domains.

Extensions for solving the three dimensional electromagnetic inverse scattering problem as well as domain sparsification schemes that make use of field and permittivity derivatives are underway.

REFERENCES

1. Pastorino, M., *Microwave Imaging*, Wiley, 2010.
2. Colton, D. and R. Kress, *Inverse Acoustic and Electromagnetic Inverse Acoustic and Electromagnetic Scattering Theory*, Springer, 2012.
3. Aster, R. C., B. Borchers, and C. H. Thurber, *Parameter Estimation and Inverse Problems*, Academic Press, 2013.
4. Bindu, G. N., S. J. Abraham, A. Lonappan, V. Thomas, C. K. Aanandan, and K. T. Mathew, "Active microwave imaging for breast cancer detection," *Progress In Electromagnetics Research*, Vol. 58, 149–169, 2006.
5. Devaney, A. J., *Mathematical Foundations of Imaging, Tomography and Wavefield Inversion*, Cambridge University Press, 2012.
6. Aftanas, M., "Through-wall imaging with UWB radar system," Department of Electronics and Multimedia Communications, Technical University of Kosice, 2009.
7. Takagi, T., J. R. Bowler, and Y. Yoshida, Eds., *Electromagnetic Nondestructive Evaluation*, IOS Press, 1997.
8. Caorsi, S., A. Massa, and M. Pastorino, "A crack identification microwave procedure based on a genetic algorithm for nondestructive testing," *IEEE Trans. Antennas Propag.*, Vol. 49, No. 12, 1812–1820, 2001.
9. Zorgati, R., B. Duchene, D. Lesselier, and F. Pons, "Eddy current testing of anomalies in conductive materials. I. Qualitative imaging via diffraction tomography techniques," *IEEE Trans. Magn.*, Vol. 27, No. 6, 4416–4437, 1991.
10. Chien, W., "Inverse scattering of an un-uniform conductivity scatterer buried in a three-layer structure," *Progress In Electromagnetics Research*, Vol. 82, 1–18, 2008.
11. Cui, T. J., W. C. Chew, A. A. Aydiner, and S. Chen, "Inverse scattering of two-dimensional dielectric objects buried in a lossy earth using the distorted Born iterative method," *IEEE Trans. Geosci. Remote Sens.*, Vol. 39, No. 2, 339–346, 2001.
12. Zhang, W., "Two-dimensional microwave tomographic algorithm for radar imaging through multilayered media," *Progress In Electromagnetics Research*, Vol. 144, 261–270, 2014.
13. Potter, L. C., E. Ertin, J. T. Parker, and M. Cetin, "Sparsity and compressed sensing in radar imaging," *Proc. IEEE*, Vol. 98, No. 6, 1006–1020, 2010.
14. Tsang, L. and J. A. Kong, and R. T. Shin, *Theory of Microwave Remote Sensing*, Wiley, 1985.

15. Rajan, S. D. and G. V. Frisk, "A comparison between the Born and Rytov approximations for the inverse backscattering," *Geophy.*, Vol. 54, 864–871, 1989.
16. Zhang, Z. Q. and Q. H. Liu, "Two nonlinear inverse methods for electromagnetic induction measurements," *IEEE Trans. Geosci. Remote Sens.*, Vol. 39, No. 6, 1331–1339, 2001.
17. Estatico, C., G. Bozza, A. Massa, M. Pastorino, and A. Randazzo, "A two-step iterative inexact-Newton method for electromagnetic imaging of dielectric structures from real data," *Inverse Problems*, Vol. 21, No. 6, S81, 2005.
18. Wang, Y. M. and W. C. Chew, "An iterative solution of the two-dimensional electromagnetic inverse scattering problem," *Int. J. of Imaging Syst. Technol.*, Vol. 1, 100–108, 1989.
19. Desmal, A. and H. Bagci, "Shrinkage-thresholding enhanced Born iterative method for solving 2D inverse electromagnetic scattering problem," *IEEE Trans. Antennas Propag.*, Vol. 62, No. 7, 3878–3884, 2014.
20. Bagci, H., R. Raich, A. E. Hero, and E. Michielssen, "Sparsity-regularized Born iterations for electromagnetic inverse scattering," *Proc. IEEE Int. Symp. Antennas and Propagation*, 1–4, 2008.
21. Desmal, A. and H. Bagci, "A preconditioned inexact Newton method for nonlinear sparse electromagnetic imaging," *IEEE Geosci. Remote Sens. Lett.*, Vol. 12, No. 3, 532–536, 2015.
22. Bozza, G. and M. Pastorino, "An inexact Newton-based approach to microwave imaging within the contrast source formulation," *IEEE Trans. Antennas Propag.*, Vol. 57, No. 4, 1122–1132, 2009.
23. Estatico, C., M. Pastorino, and A. Randazzo, "A novel microwave imaging approach based on regularization in Banach spaces," *IEEE Trans. Antennas Propag.*, Vol. 60, No. 7, 3373–3381, 2012.
24. Chew, W. C. and Y. M. Wang, "Reconstruction of two-dimensional permittivity distribution using the distorted Born iterative method," *IEEE Trans. Med. Imag.*, Vol. 9, No. 2, 218–225, 1990.
25. Franchois, A. and C. Pichot, "Microwave imaging-complex permittivity reconstruction with a Levenberg-Marquardt method," *IEEE Trans. Antennas Propag.*, Vol. 45, No. 2, 203–215, 1997.
26. Abubakar, A., T. M. Habashy, and P. M. Van den Berg, "Nonlinear inversion of multi-frequency microwave fresnel data using the multiplicative regularized contrast source inversion," *Progress In Electromagnetics Research*, Vol. 62, 193–201, 2006.
27. Zakaria, A., I. Jeffrey, and J. LoVetri, "Full-vectorial parallel finite-element contrast source inversion method," *Progress In Electromagnetics Research*, Vol. 142, 463–483, 2013.
28. Ping, X. W. and T. J. Cui, "The factorized sparse approximate inverse preconditioned conjugate gradient algorithm for finite element analysis of scattering problems," *Progress In Electromagnetics Research*, Vol. 98, 15–31, 2009.
29. Abubakar, P. M., "Contrast source inversion method: State of art," *Progress In Electromagnetics Research*, Vol. 34, 189–218, 2001.
30. Li, Y. and W. Yang, "Image reconstruction by nonlinear Landweber iteration for complicated distributions," *Meas. Sci. Technol.*, Vol. 19, No. 9, 094014, 2008.
31. Hettlich, F., "The Landweber iteration applied to inverse conductive scattering problems," *Inverse Problems*, Vol. 14, No. 4, 931–947, 1998.
32. Fornasier, M., *Theoretical Foundations and Numerical Methods for Sparse Recovery*, Walter de Gruyter, 2010.
33. Daubechies, I., M. Defrise, and C. De Mol, "An iterative thresholding algorithm for linear inverse problems with a sparsity constraint," *Commun. Pure Appl. Math.*, Vol. 57, No. 11, 1413–1457, 2004.
34. Wei, S. J., X. L. Zhang, J. Shi, and K. F. Liao, "Sparse array microwave 3-D imaging: Compressed sensing recovery and experimental study," *Progress In Electromagnetics Research*, Vol. 135, 161–181, 2013.
35. Landweber, L., "An iteration formula for Fredholm integral equations of the first kind," *Amer. J. Math*, Vol. 73, No. 3, 615–624, 1951.
36. Hanke, M., A. Neubauer, and O. Scherzer, "A convergence analysis of the Landweber iteration for nonlinear ill-posed problems," *Numerische Mathematik*, Vol. 72, No. 1, 21–37, 1995.
37. Peterson, A. F., S. L. Ray, and R. Mittra, *Computational Methods for Electromagnetics*, IEEE

Press, New York, 1998.

38. Blumensath, T. and M. E. Davies, "Iterative hard thresholding for compressed sensing," *IEEE Trans. Antennas Propag.*, Vol. 27, No. 3, 265–274, 2009.
39. Wright, S. J., R. D. Nowak, and M. A. Figueiredo, "Sparse reconstruction by separable approximation," *IEEE Trans. Signal Process.*, Vol. 57, No. 7, 2479–2493, 2009.
40. Kaltenbacher, B., A. Neubauer, and O. Scherzer, *Iterative Regularization Methods for Nonlinear Ill-posed Problems*, Walter de Gruyter, 2008.
41. Geffrin, J. M., P. Sabouroux, and C. Eyraud, "Free space experimental scattering database continuation: Experimental set-up and measurement precision," *Inverse Problems*, Vol. 21, No. 6, S117–S130, 2005.
42. Bloemenkamp, R. F., A. Abubakar, and P. M. van den Berg, "Inversion of experimental multi-frequency data using the contrast source inversion method," *Inverse Problems*, Vol. 17, No. 6, 1611–1622, 2001.